

Thermophysical modeling of Didymos' moon for the Asteroid Impact Mission

Ivanka Pelivan^{a,*}, Line Drube^a, Ekkehard Kührt^a, Jörn Helbert^a, Jens Biele^b,
Michael Maibaum^b, Barbara Cozzoni^b, Valentina Lommatsch^b

^a DLR Institute of Planetary Research, Berlin, Germany

^b DLR-MUSC, Space Operations and Astronaut Training, Cologne, Germany

Received 22 October 2016; received in revised form 27 December 2016; accepted 29 December 2016

Available online 17 January 2017

Abstract

Although typically less resolved through observations, the secondary in a binary system of asteroids is an interesting target for space missions such as the Asteroid Impact Mission. Estimates of the surface temperature distribution are important for mission design. Based on known, assumed and derived physical properties, a thermophysical model of the smaller body in the 65803 Didymos system is established. Because of the unknown thermal inertia, a parameter study has been carried out for a thermal inertia range of $\Gamma = 50\text{--}1000 \text{ J m}^{-2} \text{ K}^{-1} \text{ s}^{-1/2}$. Results are presented for the minimum and maximum values of this range and a likely value of $\Gamma = 500 \text{ J m}^{-2} \text{ K}^{-1} \text{ s}^{-1/2}$. The parameter study extends from the unshadowed to the eclipsed case where shadowing through the primary is simulated in a simplified manner assuming that the orbit of the moon lies in the equatorial plane of the primary with its z -axis normal to this plane. Results from this study are used to investigate performance for instruments foreseen for the Asteroid Impact Mission. Preliminary results are obtained for the signal-to-noise ratio of a proposed thermal infrared imager. Furthermore, MASCOT-2 Lander thermal survivability has been investigated for several possible landing sites and specific settings.

© 2017 COSPAR. Published by Elsevier Ltd. All rights reserved.

Keywords: Asteroid thermophysical modeling; Binary asteroid system; AIM mission; MASCOT; Thermal infrared imager

1. Introduction

Binary systems are frequent among the near-Earth asteroid (NEA) population: The fraction of binaries larger than 300 m was estimated to be $15 \pm 4\%$ by [Pravec et al. \(2006\)](#). The study of binary systems is important for space missions, such as the Asteroid Impact Mission (AIM), that target the primary or secondary asteroidal body. The binary nature of Apollo class asteroid 65803 Didymos (1996 GT) was discovered in 2003 by [Pravec et al. \(2003\)](#). Didymos is a close binary system, consisting of a larger primary (780 m diameter $\pm 10\%$) and a smaller (163 m ± 18 m

across) secondary ([Michel et al., 2016](#)). Didymos' heliocentric eccentricity is reported as 0.38, the semi-major axis is 1.64 AU and the inclination to the ecliptic is 3.4 degrees.

The basic properties of the main body in the Didymos system are well characterized through photometric and radar observations ([Pravec et al., 2003](#); [Pravec et al., 2006](#); [Margot et al., 2015](#)). [Margot et al. \(2015\)](#) note that of all secondary orbital periods known so far, that of Didymos is among the shortest with a value of 11.9 h. While the rotational period of the main body is determined as 2.6 h, the secondary's rotational period could not be derived reliably. A synchronous rotation appears however compatible with observations, i.e. a rotational period equal to the secondary orbital period is assumed ([Pravec et al., 2006](#)).

* Corresponding author.

E-mail address: Ivanka.Pelivan@dlr.de (I. Pelivan).

Physical properties of 65803 Didymos have been compiled in an ESA document ([Asteroid Impact Mission: Didymos reference model, 2015](#)) for preliminary design studies (also used as main reference for the current study) of the joint ESA-NASA Asteroid Impact and Deflection Assessment (AIDA) mission. AIM is the ESA-led part of AIDA to characterize Didymos and then assess the consequences of an impact by a NASA provided spacecraft named DART (Double Asteroid Redirection Test) on the secondary in the Didymos system. During the proximity operations foreseen in 2022, the Lander MASCOT-2 (Mobile Asteroid Surface Scout-2, [Ho et al., 2016](#)), one of the payloads onboard AIM, is expected to operate approximately three months once deployed on the surface of the secondary asteroid. Modeling the daily temperature variation of Didymos' moon throughout the mission is important to investigate the thermal survivability of the MASCOT-2 Lander during on-asteroid operations and for predicting the output of the AIM thermal infrared imager. At a later stage, during or after the mission, thermophysical modeling may prove very useful in analyzing data.

The thermal emission of the secondary in a binary asteroid system depends on the secondary's shape, size, spin vector, albedo, solar distance, surface roughness, and thermal inertia, as well as the shadowing effect, reflected and thermal radiation from the primary. All these parameters can be included in a thermophysical model to predict the moon's thermal emission. Thermophysical modeling of Didymos' secondary ("Didymoon") is performed based on the current best knowledge of the physical properties of the moon as compiled in [Asteroid Impact Mission: Didymos reference model \(2015\)](#). Due to the up to now unknown thermal inertia Γ , the broad range of $\Gamma = 50\text{--}1000 \text{ J m}^{-2} \text{ K}^{-1} \text{ s}^{-1/2}$ is covered in simulation. Asteroids comparable to Didymoon in size have a globally averaged thermal inertia in the range of $100\text{--}1000 \text{ J m}^{-2} \text{ K}^{-1} \text{ s}^{-1/2}$ ([Delbo et al., 2015](#)). Locally (on a lander horizon scale), there could be dusty spots with an even lower thermal inertia; thus, we assume $\Gamma = 50 \text{ J m}^{-2} \text{ K}^{-1} \text{ s}^{-1/2}$ as the lower limit.

2. Thermophysical model

2.1. Theory

As knowledge of the physical properties of the moon is very limited at the moment, we used a relatively simple thermophysical model for an ellipsoidal body to provide longitude dependence. The asteroid's shape enters through the upper boundary condition as expanded below. The model solves the one-dimensional heat conduction Eq. (1).

$$\rho c_p \frac{\partial T(x, t)}{\partial t} = \frac{\partial}{\partial x} \left(\kappa \frac{\partial T(x, t)}{\partial x} \right) \quad (1)$$

Here ρ is the density, c_p the specific heat capacity and κ is the thermal conductivity which may be temperature-dependent but for the current state of knowledge set constant.

An adiabatic lower boundary is assumed by setting the temperature gradient to zero several annual thermal skin depth below the asteroid's surface where the skin depth is defined as $l_s = \sqrt{\kappa p_{orbit} / (\pi \rho c_p)}$ and p_{orbit} is the asteroid's orbital period. In fact at this depth the asteroid's core temperature changes very slowly such that this assumption provides a good approximation for the lower boundary of the numerical domain.

The upper boundary condition is implemented to fulfill the conservation of energy with solar insolation depending on local coordinates, time, heliocentric distance and season,

$$\frac{F_s(1-A)\cos\zeta(t)}{r_H^2(t)} = \epsilon\sigma T^4 + \kappa \frac{dT}{dx} \quad (2)$$

where F_s is the solar constant, A is the Bond albedo, ζ is the solar incidence angle, r_H is the heliocentric distance, ϵ is the thermal emissivity, σ is the Stefan-Boltzman constant, and dT/dx is the vertical temperature gradient with x positive downward.

The solar incidence angle ζ in the upper boundary condition is either evaluated based on an analytical formulation (see e.g. [Sekanina \(1979\)](#), [Gortsas et al. \(2011\)](#) for a spherical body) or, if a more complex shape model is used, based on the normal vector of the shape model facets. [Fig. 1](#) shows a simple shape model of an ellipsoid. The surface grid defines the single facets. By calculating the facet normals \underline{e}_N and the normal vector to the Sun \underline{e}_{sun} , the solar incidence angle per facet is simply

$$\cos\zeta = \underline{e}_{sun} \cdot \underline{e}_N \quad (3)$$

Depending on the number of facets, the solution to Eq. (1) can take a considerable amount of time. For an ellipsoidal shape, an analytical expression is derived from Eq. (3), see also [Kührt and Giese \(1989\)](#),

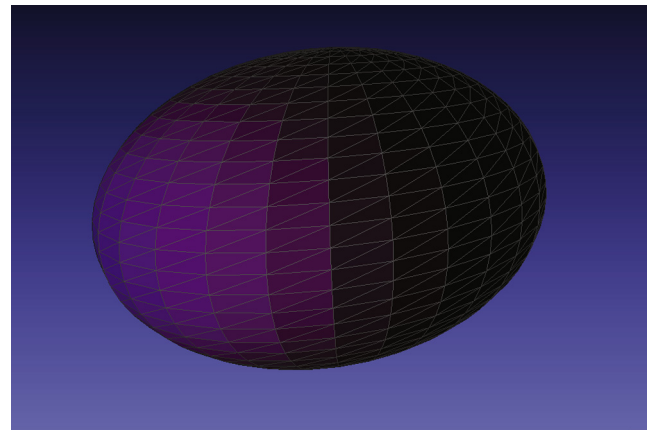


Fig. 1. Shape model of an ellipsoid. The grid shows the single facets.

$$\cos\zeta = D^{-1} \left(\frac{\cos\varphi \cdot \cos\beta \cdot \cos\varphi_S \cdot \cos\beta_S}{a^2} + \frac{\cos\varphi \cdot \sin\beta \cdot \cos\varphi_S \cdot \sin\beta_S}{b^2} + \frac{\sin\varphi \cdot \sin\varphi_S}{c^2} \right), \quad (4)$$

$$D = \left[\left(\frac{\cos\varphi \cdot \cos\beta}{a^2} \right)^2 + \left(\frac{\cos\varphi \cdot \sin\beta}{b^2} \right)^2 + \left(\frac{\sin\varphi}{c^2} \right)^2 \right]^{\frac{1}{2}},$$

where φ and β are the latitude and longitude of the asteroid and φ_S and β_S are the latitude and longitude of the Sun. Latitudes range from -90° to $+90^\circ$ while longitudes start at 0° running to $+360^\circ$. The reference frame is body fixed and originates in the secondary's center of mass. The x -axis is in the direction of the primary, the z -axis is normal to the orbital plane and the y -axis completes the right-handed system.

The surface is considered smooth in the calculations discussed in Section 3.1 below. While radiation from Didymos' primary is neglected in this first study, the shadowing effect due to solar eclipses by the primary has a strong effect on temperature evolution. Eclipses are included in the model under the assumption that the orbit of the moon lies in the equatorial plane of the primary with its z -axis normal to this plane. Simulations are performed with or without eclipse conditions. Eclipse conditions are incorporated following Kürt and Giese (1989). Therefore, beginning and end of eclipse are strictly valid for zero longitude and latitude and slightly different for other points on the ellipsoid.

In first modeling the secondary of the Didymos system, a parameter study has been carried out for different thermal inertia $\Gamma = \sqrt{\kappa\rho c_p}$. Output is saved in steps of 0.1 AU for a full orbit and for 5-degree steps in longitude and latitude. An overview of the cases for which results are presented in Section 3.1 can be found in Table 1.

Other parameters used in this study correspond to reference values compiled in Asteroid Impact Mission: Didymos reference model (2015) such as an obliquity of 171 ± 9 degrees. To investigate the effect of obliquity, the extreme case of 162 degrees has been chosen with the corresponding orbital pole $L_{orb} = 310$ degrees, $B_{orb} = -75$ degrees. The orbit period of the secondary around the primary as well as the rotation rate is set to 11.92 hours. In solving Eqs. (1) and (2), $\rho = 2146 \text{ kg m}^{-3}$, $c_p = 600 \text{ J K kg}^{-1}$ and κ is chosen such that the thermal inertias listed in Table 1 are given. The Bond albedo in

Eq. (2) is set to 0.07, corresponding to a geometric visible albedo of $p_V = 0.15$. Both geometric and Bond albedo are assumed to be identical for primary and secondary. The Bond albedo is calculated using the relation $A = qp_V$ where q is the phase integral as used in [Bowell et al. \(1979\)](#) with slope $G = 0.20$ derived by [Kitazato et al. \(2004\)](#). The value adopted for ϵ is 0.9. Results discussed in the next section refer to an ellipsoid with major axis $a = 103 \text{ m}$ and minor axes $b = 79 \text{ m}$ and $c = 66 \text{ m}$.

2.2. Model discussion

Didymos' secondary is modeled in a simplified manner due to the many unknowns and assumptions adopted in this study. This section deals with neglected effects thought to alter surface temperatures in certain cases.

When applying the one-dimensional heat conduction equation, obviously heat flow perpendicular to the radial direction is neglected. This is justified if the radial thermal conduction is effective over length scales significantly below the resolution of the asteroid's shape model. To estimate this, the diurnal thermal skin depth $l_{s,d} = \sqrt{\kappa p_{rot}/(\pi\rho c_p)}$, where p_{rot} is the rotation period of the asteroid, is compared to the mean distance d_{grid} between latitudinal and longitudinal grid points. Even for the highest thermal inertia employed, the ratio $l_{s,d}/d_{grid} \ll 1$ and therefore only one-dimensional heat flow can be considered.

A complete thermophysical model includes diffuse solar radiation as well as direct and diffuse self-heating that enter in the upper boundary condition as

$$U + W + u + w = \epsilon\sigma T^4 + \kappa \frac{dT}{dx}, \quad (5)$$

where the direct solar flux U is the left-hand term in Eq. (2)

$$U = \frac{F_S(1-A)\cos\zeta(t)}{r_H^2(t)}. \quad (6)$$

The formulations for the diffuse solar radiation W as well as the direct and diffuse thermal self-heating u and w depend on the usage of a single- or multiple-scattering mode ([Davidsson and Rickman, 2014](#)). For the current simplified model of an ellipsoid these terms do not contribute and have therefore not been included in the calculation. Eq. (5) has to be used with a more complex shape model and to include radiative transfer between the moon and the primary. The mutual heating from the primary has been assessed mostly as small due to the comparatively large distance of 1.18 km ([Asteroid Impact Mission: Didymos reference model, 2015](#)) between the primary and the moon (large when compared to meter-length distance between grid points on the moon). Heating from the primary enters through terms W_p, u_p and w_p depending on the areas of the primary that are in view to the secondary (subscript p refers to "primary" when applying the corresponding terms from Eq. (5)). Due to the low albedo, the single-scattering mode is applied for which the diffuse thermal heating flux w_p can be neglected. Discretizing the

Table 1
Case study for Didymos' secondary.

Case	Thermal inertia	Eclipse condition
1	50	Off
2	500	Off
3	1000	Off
4	50	On
5	500	On
6	1000	On

secondary into facets j and the primary into facets i , the mutual heating contribution from diffuse solar radiation from the primary can be expressed as

$$W_{p,j} = \sum_{i \neq j}^N V_{ij} \frac{F_s A \cos \zeta_j(t)}{r_H^2(t)} v_{j, \text{Sun}}. \quad (7)$$

N is the total number of facets, $v_{j, \text{Sun}}$ is the facet view factor to the Sun, and V_{ij} is the view factor describing the fraction of energy emitted from one facet towards another,

$$V_{ij} = \frac{a_i \cos \Theta_i \cos \Theta_j}{\pi r^2}. \quad (8)$$

Here a_i is the surface area of element i , r is the distance between facets i and j , and the angles Θ are the angles between the facet outward normal and the line between facet centers. The viewing factor $V_{ij} = 0$ if the line of sight is intercepted by topography or if Θ_i or Θ_j are $\geq 90^\circ$.

Due to the low Bond albedo, direct thermal heating from the primary is considered as the largest flux from the primary,

$$u_{p,j} = \sum_{i \neq j}^N V_{ij} \epsilon \sigma T_{s,i}^4. \quad (9)$$

$T_{s,i}$ is the surface temperature of facet i .

Mutual heating based on the view factors from Eq. (8) is displayed in Fig. 2. The colors green and blue in Fig. 2 refer to larger resulting fluxes where the actual values have been enhanced to make the effect visible.

The actual fluxes based on the viewing factors between the primary and the moon have not been calculated exactly but an upper limit has been derived, taking maximum

surface temperatures from the moon as input from the primary, assuming that both secondary and primary have the same thermal inertia of $\Gamma = 500 \text{ J m}^{-2} \text{ K}^{-1} \text{ s}^{-1/2}$. In fact, Michel et al. (2016) show that daytime temperatures at perihelion, using a thermal inertia of $\Gamma = 700 \text{ J m}^{-2} \text{ K}^{-1} \text{ s}^{-1/2}$, are lower for Didymos' primary than for its secondary due to the different rotation periods. Applying maximum daytime temperatures from the moon on all moon-facing facets of the primary, the resulting possibly occurring maximum fluxes due to mutual self-heating are typically at least two orders of magnitude smaller than fluxes from direct solar irradiation on the moon. This however is based on the presence of all fluxes. In the case where the night side of the moon is facing the day side of the primary, heating from the primary will affect the night-side temperatures of the secondary. Given the above worst case assumption of a uniformly hot primary surface, the highest incoming flux will occur at the position on the moon where the normal vector of the surface area directly points at the primary's center (i.e. latitude = longitude = 0), collecting fluxes from all facets in the field of view within $[-90, 90]$ degrees. Any surface area on the secondary further away from this point will receive less heating from the primary. In Fig. 3 viewing factors for an example facet on the Moon slightly off the center point facing the primary are shown.

As temperatures of the primary are not computed, all facet temperatures $T_{s,i}$ from Eq. (9) are set to the same high value based on midday temperatures of the moon. In applying Eqs. (9) and (7) therefore an upper limit is derived for the occurring fluxes W_p and u_p . The temperature change due to heating from the primary is evaluated by applying Eq. (5) which for the night side of the moon reduces to

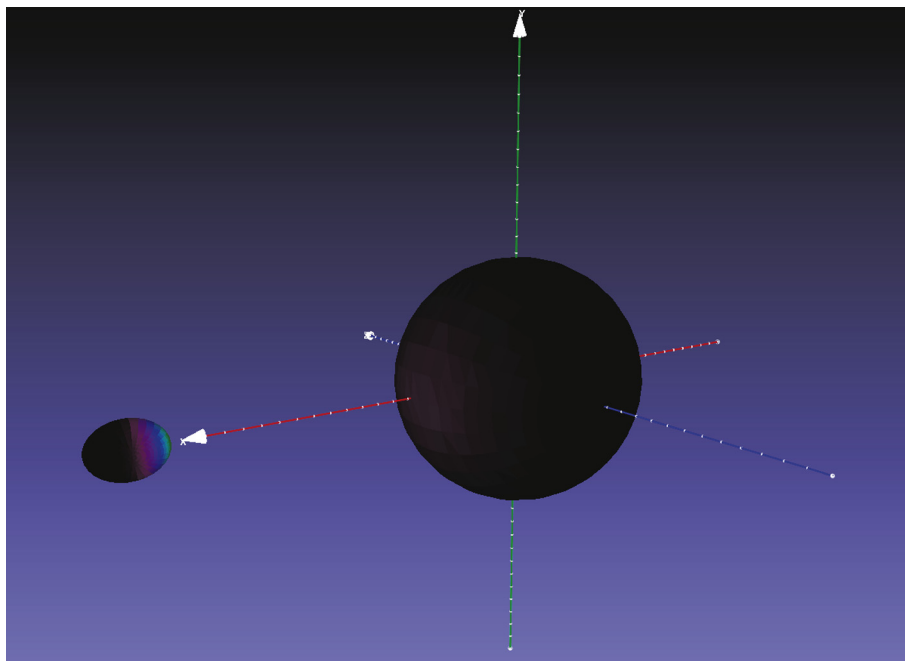


Fig. 2. Mutual heating of binary system model.

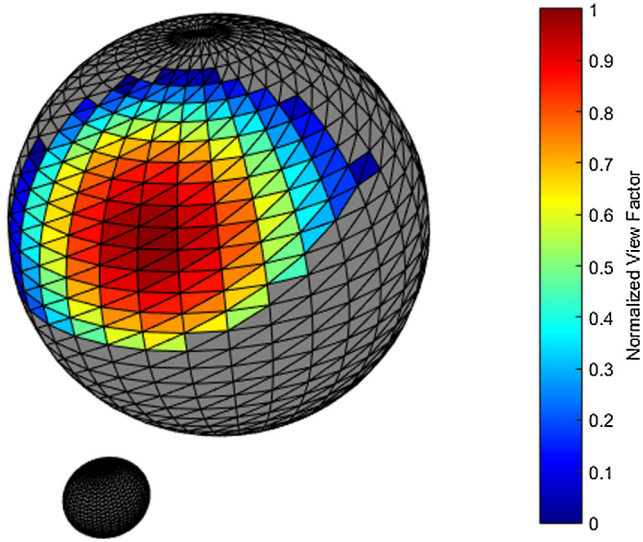


Fig. 3. Normalized viewing factors for a facet on the moon slightly off latitude = longitude = 0 degree. All colored facets on the primary contribute to a temperature rise on the moon's facet. (For interpretation of the references to colour in this figure legend, the reader is referred to the web version of this article.)

$$W_p + u_p = \epsilon \sigma T^4 + \kappa \frac{dT}{dx}. \quad (10)$$

The last term in Eq. (10) is so small that it has not been re-evaluated. The temperatures derived from Eq. (10) are compared to the corresponding temperatures from the basic model introduced in Section 2.1 to evaluate the maximum effect of heating from the primary.

The effect of heating from the primary on the night side of the moon is shown in Fig. 4 (left) where the absolute difference between temperatures including and neglecting heating from the primary, normalized with the midnight temperature of the moon (without heating from the primary) is displayed. Fluxes from the primary may alter temperatures by up to 4.5% at perihelion. In comparison,

temperature differences when applying low and intermediate thermal inertia values in the basic model, amount to more than 30% at perihelion and more than 20% near aphelion for nighttime temperatures, see Fig. 4 (right).

It has to be noted that the effect shown in Fig. 4 (left) will be higher if temperatures on the primary are larger than the assumed ones, e.g. if the primary has a smaller thermal inertia than the moon.

Surface roughness may be resolved in a finely discretized shape model. If possible, e.g. from highly resolved imaging, the application would be numerically very demanding. Unresolved surface roughness has a large effect on the brightness temperature in radiometric observations (Kührt et al., 1992; Davidsson et al., 2015). Surface roughness has not been considered in the current model mainly due to unknown surface properties. In modeling unresolved surface roughness, different approaches may be followed as outlined in Davidsson et al. (2015). In a small sample study, we focus on the most common type of model roughness, i.e. the spherical segment. As described in Kührt et al. (1992), a crater opening angle of 180 degrees is used to model half spheres. Fig. 5 shows a typical temperature distribution within a half sphere with shadowing effects clearly visible.

In evaluating the effect of surface roughness on brightness temperature, sample runs were performed for a Sun incidence angle of 0 (no crater shadowing), 30 degrees (see Fig. 5), and 60 degrees (crater mostly shadowed) for thermal inertia of $\Gamma = 50$ and $\Gamma = 500 \text{ J m}^{-2} \text{ K}^{-1} \text{ s}^{-1/2}$ near perihelion, near aphelion, and inbetween. As the discretization of the spherical segment is such that it cannot be resolved by an imaging instrument at spacecraft distance, we calculate the distribution of kinetic temperatures, from which brightness temperatures as observed by an example detector can be derived. For the comparison of a Lambertian surface with a rough one, the following detector specifics were used: The angle between the detector and surface normal of the crater cover is set to 0, and the

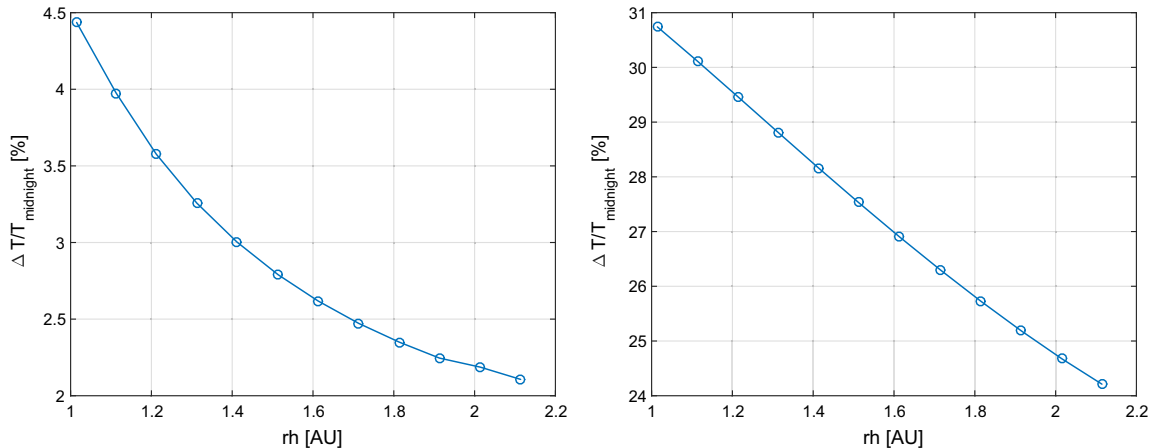


Fig. 4. Relative surface temperature changes at latitude = longitude = 0 degrees. Left: changes due to thermal heating from the primary, right: changes due to uncertainty in thermal inertia (compared are $\Gamma = 50$ and $\Gamma = 500 \text{ J m}^{-2} \text{ K}^{-1} \text{ s}^{-1/2}$). T_{midnight} is the temperature on the night side of the moon without thermal heating from the primary for a thermal inertia of $\Gamma = 500 \text{ J m}^{-2} \text{ K}^{-1} \text{ s}^{-1/2}$.

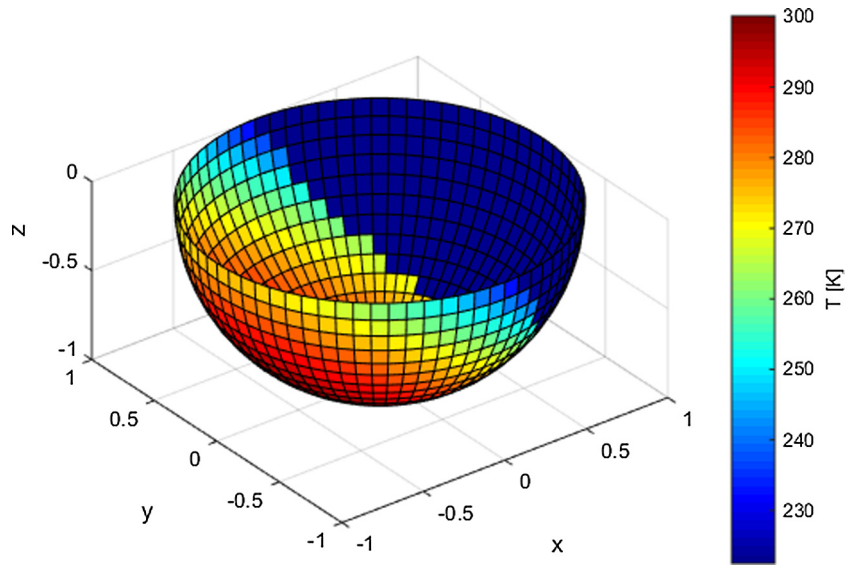


Fig. 5. Distribution of kinetic temperatures in a spherical crater. The incident angle of the Sun is 30 degrees.

effective wavelength of the sensor is set to $5\ \mu\text{m}$. The difference between brightness temperatures of a smooth and a cratered surface, normalized with the temperature of the smooth surface, is shown in Fig. 6. The deviation from the smooth surface is typically below 5% except for one case.

For a low thermal inertia, surface roughness is more important than for a higher value. However, a study comprising a small number of sample points naturally is not conclusive, furthermore, seemingly existing trends also depend on the detector characteristics applied. It can however be said that surface roughness may lead to a significant change in (brightness) temperatures.

3. Application and results

3.1. Model results

Model calculations have been performed for the temperature evolution of Didymos' secondary along the full orbit for different thermal inertia assuming an ellipsoidal shape. Results are presented for the lower and upper limit considered and a likely intermediate value, i.e. for $\Gamma = 50, 500$ and $1000\ \text{J m}^{-2}\ \text{K}^{-1}\ \text{s}^{-1/2}$. A few examples of the results without eclipse can be found in Figs. 7 and 9. Including shadowing effects of the primary generally leads to lower maximum temperatures as can be seen in Figs. 8 and 10.

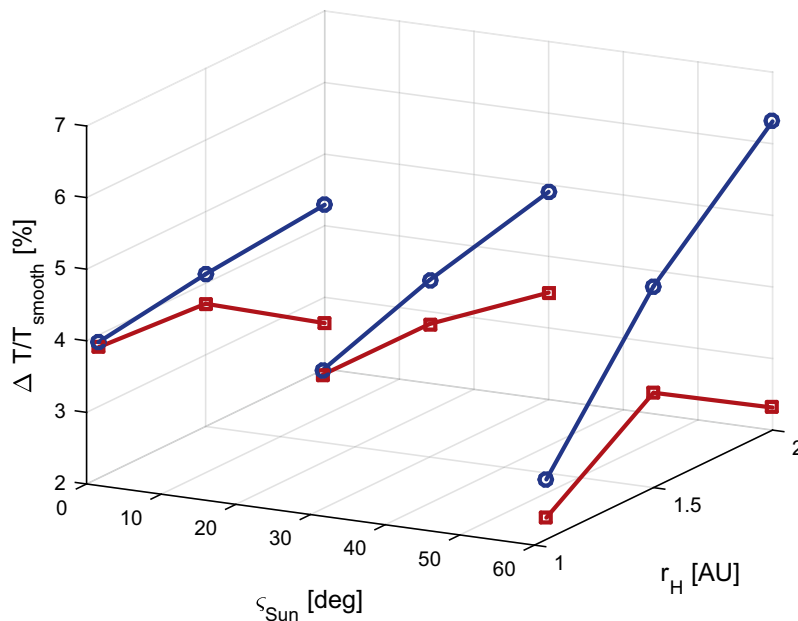


Fig. 6. Difference in measured temperatures between smooth and rough surfaces for sample points in orbit. Round symbols correspond to a thermal inertia of $\Gamma = 50\ \text{J m}^{-2}\ \text{K}^{-1}\ \text{s}^{-1/2}$, squares show results for $\Gamma = 500\ \text{J m}^{-2}\ \text{K}^{-1}\ \text{s}^{-1/2}$.

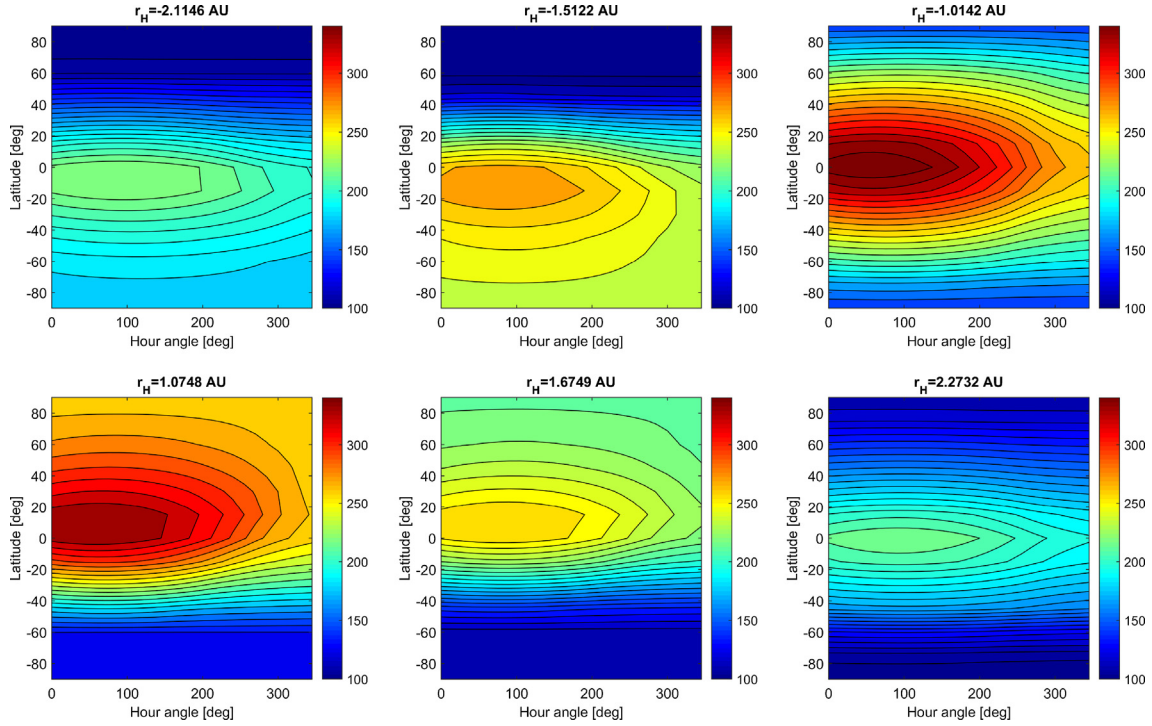


Fig. 7. Contour maps of the daily surface temperature [K] variation at longitude = 0 degree on Didymos' secondary for the case of a thermal inertia of $\Gamma = 500 \text{ J m}^{-2} \text{ K}^{-1} \text{ s}^{-1/2}$. Contour maps for six different solar distances r_H are shown. The northern winter can be seen in the first two and the northern summer in the 4th and 5th plot (from left to right). The spin axis is given as 171 ± 9 degrees (Asteroid Impact Mission: Didymos reference model, 2015). Here, the extreme case of 162 degrees has been used.

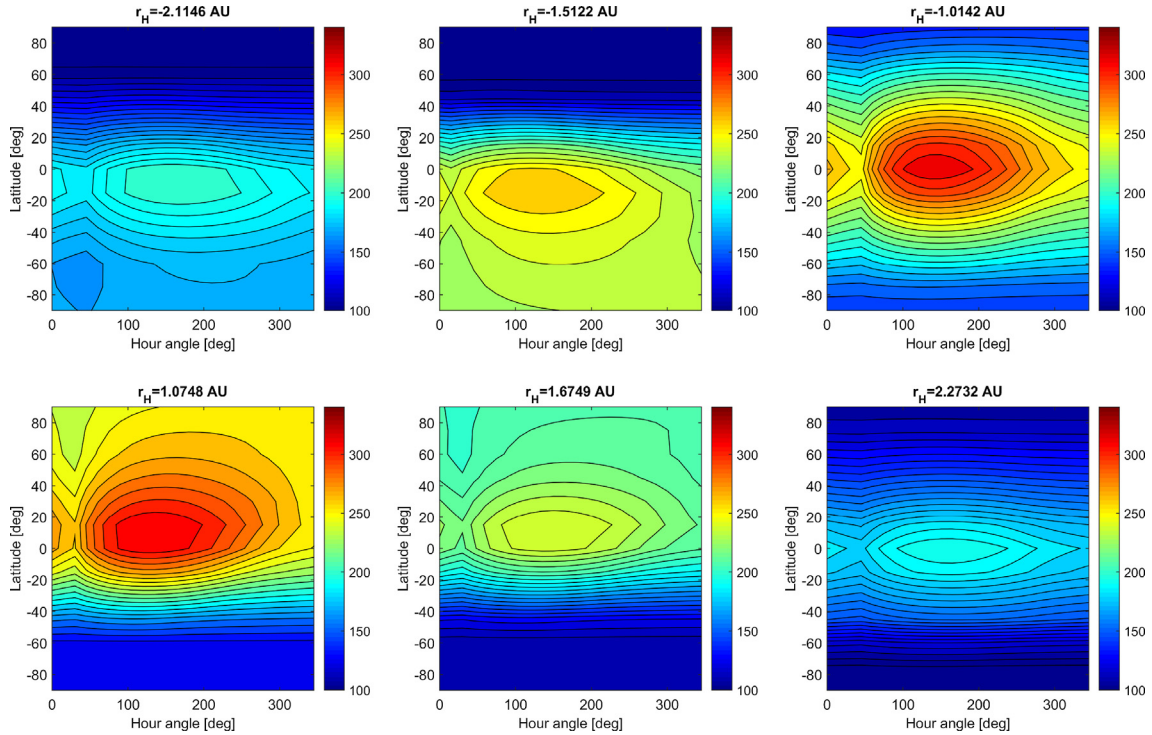


Fig. 8. Contour maps of the daily surface temperature [K] variation at longitude = 0 degree on Didymos' secondary for the case of a thermal inertia of $\Gamma = 500 \text{ J m}^{-2} \text{ K}^{-1} \text{ s}^{-1/2}$. Same configuration as shown in Fig. 7 but with eclipse included.

Figs. 7 and 8 show temperature maps for a fixed longitude (0 degrees) and several distances to the Sun covering near-perihelion and aphelion. Negative distances denote

the incoming orbit leg. As expected, highest temperatures are reached near perihelion. The obliquity effect is strongly visible: While at perihelion the highest temperatures can be

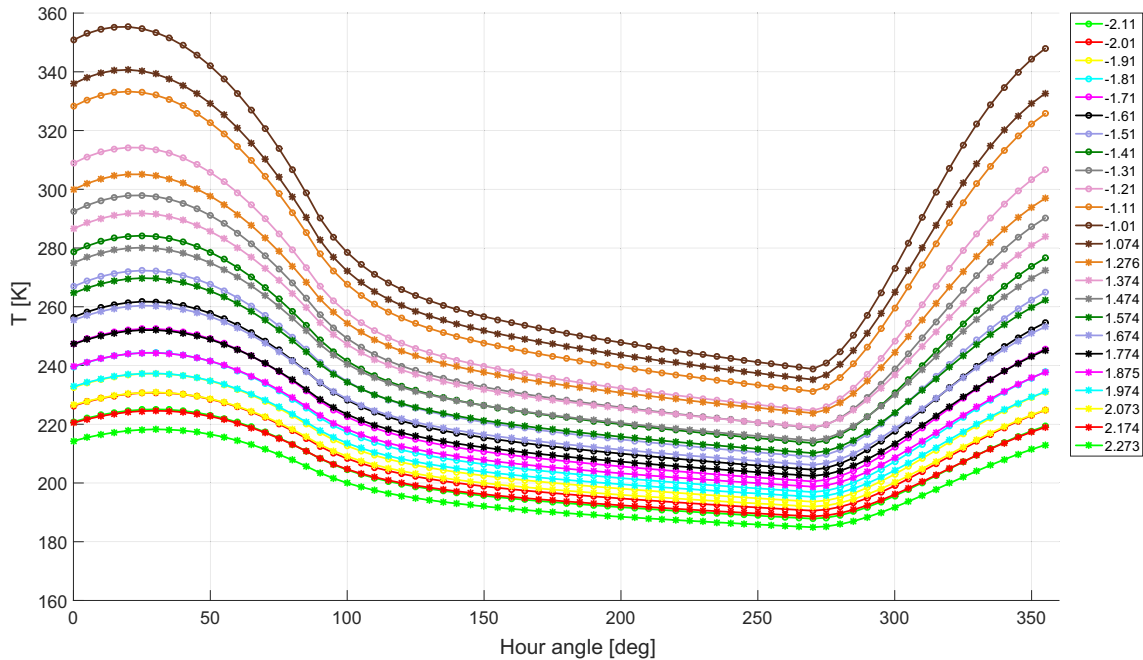


Fig. 9. Surface temperatures for a thermal inertia of $\Gamma = 500 \text{ J m}^{-2} \text{ K}^{-1} \text{ s}^{-1/2}$ at latitude = longitude = 0 degrees. The legend shows the heliocentric distance r_H in AU where -AU denotes the incoming orbit leg.

observed around zero latitude, temperature peaks shift to higher latitudes with increasing distance towards aphelion. Passing aphelion, temperature peaks move to lower latitudes. Eclipse effects occur with a phase delay and cause a strong temperature drop for a limited amount of time and an overall decrease in minimum and maximum temperatures, see also Fig. 10.

The diurnal temperature variation for all output distances investigated is shown in Figs. 9 and 10 for zero latitude and longitude and a thermal inertia of $\Gamma = 500 \text{ J m}^{-2} \text{ K}^{-1} \text{ s}^{-1/2}$. These are typical trends for convex asteroid shapes without obstructed surface elements. A lower thermal inertia leads to higher peak temperatures past noon and lower nightside temperatures while curves for higher thermal inertia show a lesser spread between minimum and maximum temperatures. At large distances the spread between day- and nightside is less pronounced than closer to the Sun.

Peak temperatures are plotted in Fig. 11 for all thermal inertia considered. The top figures show the maximum temperatures for each heliocentric distance for which an output has been computed. The phase delay observed in the diurnal temperature variation increases with increasing heliocentric distance for the case of unobstructed illumination and also occurs at a later time of day for increasing thermal inertia (see bottom left of Fig. 11). It is interesting to note that in the eclipsed case, the highest temperatures may occur just before the primary shadows the moon. This always happens for the lowest thermal inertia investigated of $\Gamma = 50 \text{ J m}^{-2} \text{ K}^{-1} \text{ s}^{-1/2}$ and less often for increased thermal inertia, i.e. in some cases surface temperatures do not reach a temperature maximum after noon.

A direct comparison of maximum as well as minimum temperatures for the different thermal inertia is provided in Fig. 12. The comparison is carried out for the equator of Didymos' secondary with and without eclipse ("E." in the label means that eclipse is included) for different solar distances. For the high thermal inertia case ($\Gamma = 1000 \text{ J m}^{-2} \text{ K}^{-1} \text{ s}^{-1/2}$) the maximum and minimum temperatures are significantly lower when eclipses are included in the calculation, while in the low thermal inertia case of $\Gamma = 50 \text{ J m}^{-2} \text{ K}^{-1} \text{ s}^{-1/2}$ there is only a slight difference. The minimum and maximum temperatures were taken from the the daily variation shown in Figs. 9 and 10.

3.2. Application to thermal infrared imager

A thermal infrared imager (TIRI) has been foreseen as part of the AIM baseline payload (Michel et al., 2016). A TIRI is useful to characterize the surface and regolith of an asteroid by measuring the thermal behavior of the body. In order to decide which wavelength region the thermal infrared imager should observe in, it has to be measured or estimated at which wavelengths the asteroid emits most of its thermal energy. In the lack of measurements, a thermophysical model of the asteroid can be utilized with appropriate physical parameters to investigate the thermal behavior. Using the model cases listed in Table 1, the peak emission was obtained from daily maximum and minimum surface temperatures at the equator throughout the mission (see Fig. 12), by calculating the spectral radiance of the surface for a range of wavelengths using Planck's law (assuming the asteroid radiates like a blackbody). The wavelengths of the peak spectral radiance for different solar

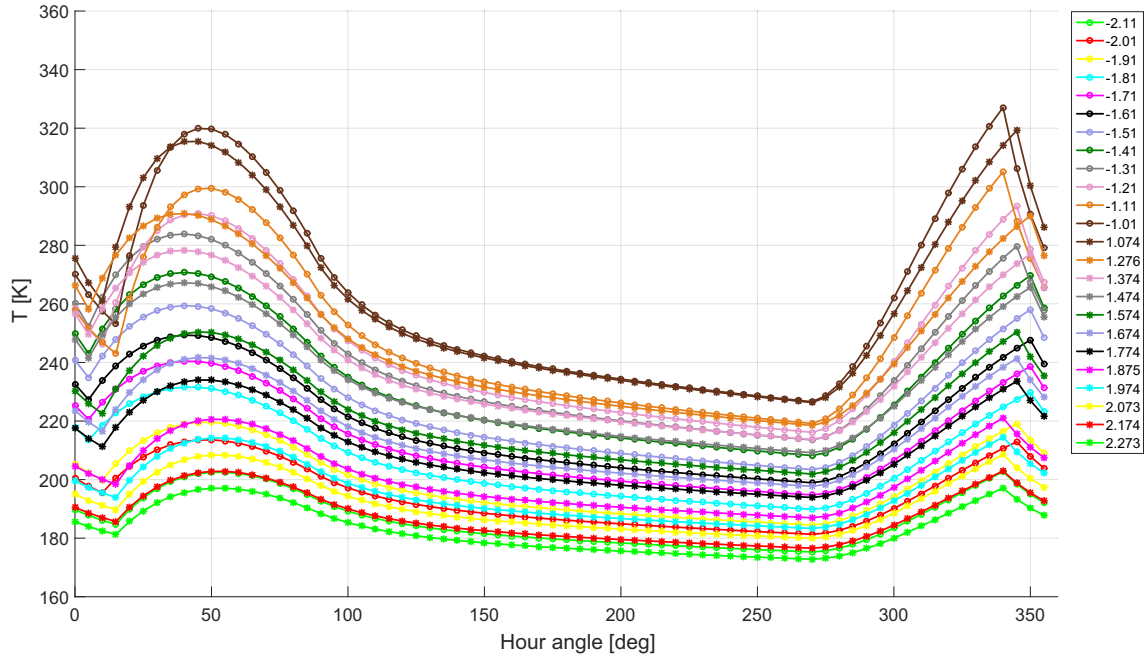


Fig. 10. Surface temperatures for a thermal inertia of $\Gamma = 500 \text{ J m}^{-2} \text{ K}^{-1} \text{ s}^{-1/2}$ at latitude = longitude = 0 degrees. Same configuration as shown in Fig. 9 but with eclipse included.

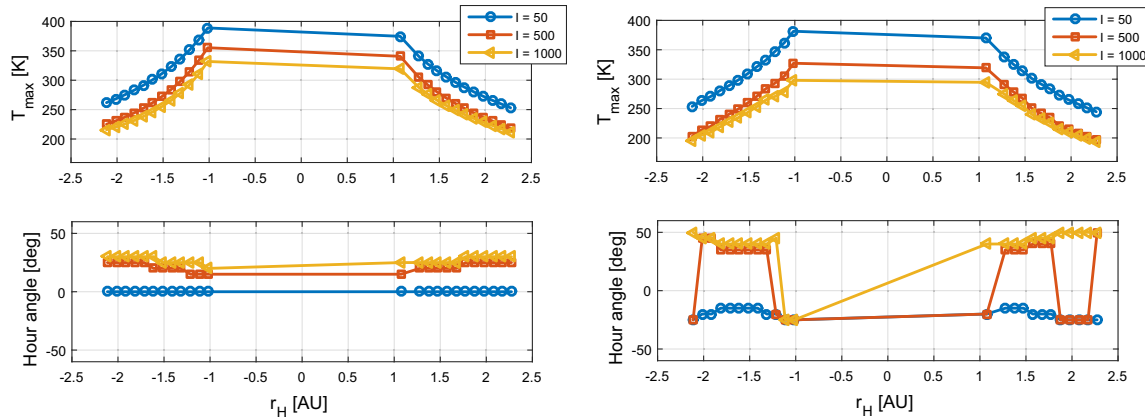


Fig. 11. Maximum surface temperatures for three thermal inertia at latitude = longitude = 0 degrees (left: no eclipse, right: with eclipse). Top figures show the temperatures and bottom figures show at which hour angle they occur for each heliocentric distance considered. For better readability, an hour angle range of $[-180, 180]$ instead of $[0, 360]$ (clipped above 50 and below -50 degrees) is used.

distances along the orbit and for several thermal inertia with or without eclipse included can be seen in Fig. 13. In Figs. 12 and 13, extrema for thermal inertia of $\Gamma = 50, 500$ and $1000 \text{ J m}^{-2} \text{ K}^{-1} \text{ s}^{-1/2}$ are shown. These figures also show the non-linearity of the peak wavelength with thermal inertia. For thermal inertia of $\Gamma = 500$ and $1000 \text{ J m}^{-2} \text{ K}^{-1} \text{ s}^{-1/2}$ the peak is around $9\text{--}16 \mu\text{m}$ during the mission and $7\text{--}22 \mu\text{m}$ in the case of $\Gamma = 50 \text{ J m}^{-2} \text{ K}^{-1} \text{ s}^{-1/2}$.

One of the TIRIs proposed for the AIM spacecraft is based on the MERTIS (Mercury Radiometer and Thermal Infrared Spectrometer, see e.g. Walter et al., 2011) instrument which is part of the BepiColombo mission. MERTIS combines an IR-spectrometer in the wavelength range of $7\text{--}14 \mu\text{m}$ with a radiometer operating in the wavelength

region of $7\text{--}40 \mu\text{m}$. Applied to the current estimates, this combination would cover the peak as well as the tail of the asteroid's Planck curve.

To calculate the spectral irradiance arriving at the spacecraft from the moon, Planck's law of blackbody radiation is used for the temperature of each surface element. It is assumed that the radiation is emitted into a hemisphere as a Lambertian surface with θ being the angle of emission. The thermally emitted spectral flux f_{IR} at a 1 m^2 area perpendicular to the direction of the center of Didymoon at the spacecraft distance r_{sc} [m] is computed by adding up the emitted spectral radiance I_{ast} [$\text{W } \mu\text{m}^{-1} \text{ m}^{-2} \text{ sr}^{-1}$], for each of the surface elements a_{ast} visible from the given spacecraft position (Delbo et al., 2015), taking into account the tilt ψ of the 1 m^2 area as seen from the surface element:

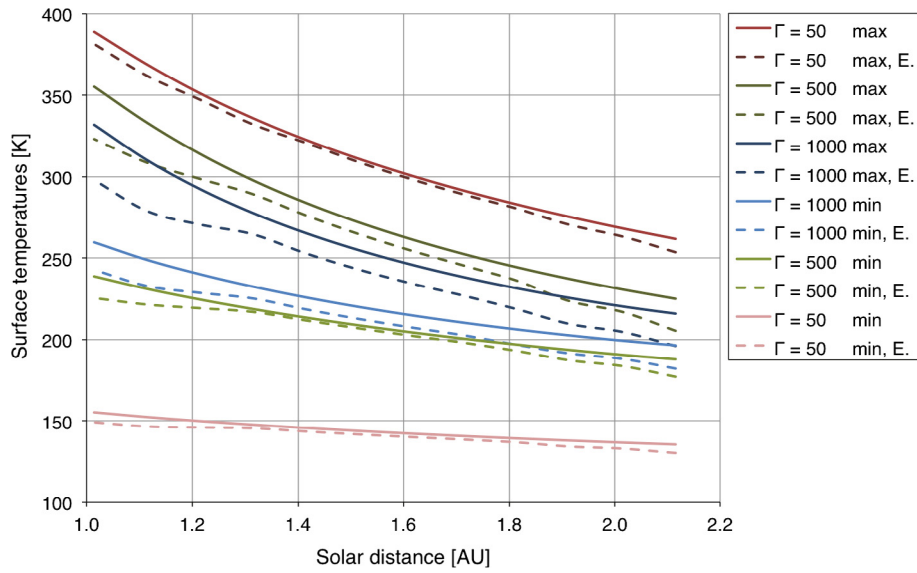


Fig. 12. Daily variations in the minimum/maximum temperatures at the equator of Didymos' secondary with and without eclipse ("E." denotes that eclipse is included).

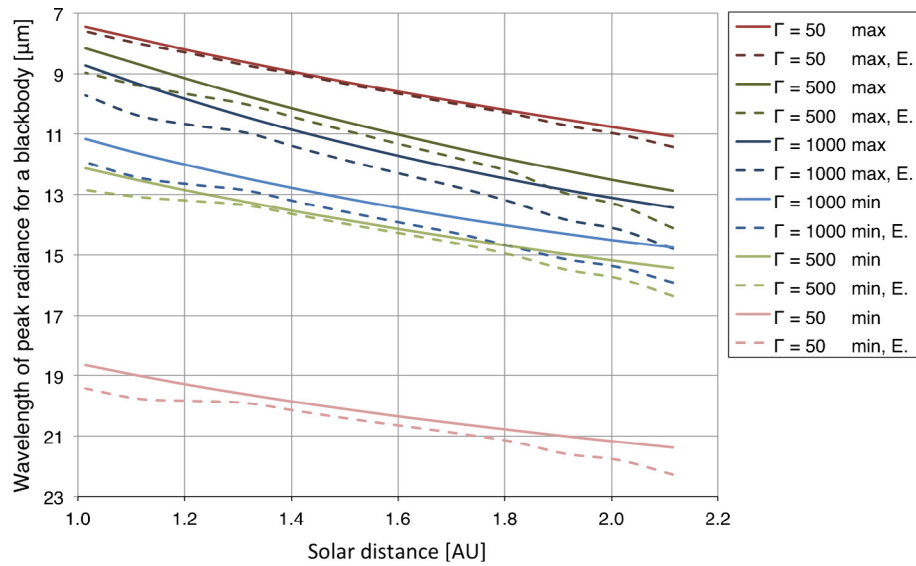


Fig. 13. Daily variations in the wavelength of peak radiance for minimum/maximum temperatures at the equator of Didymos' secondary with and without eclipse ("E." denotes that eclipse is included).

$$f_{IR} = \sum \epsilon I_{ast} \cos(\Theta) \cos(\Psi) a_{ast}/r_{sc}^2 \quad (11)$$

where a_{ast}/r_{sc}^2 is the solid angle [sr] subtended by the 1 m^2 area at the distance r_{sc} . The unit of f_{IR} is therefore $\text{W } \mu\text{m}^{-1} \text{ m}^2$. The total spectral flux [$\text{W } \mu\text{m}^{-1} \text{ m}^{-2}$] is a combination of the thermally emitted and the reflected solar radiation. The solar spectral flux P [$\text{W } \mu\text{m}^{-1}$] arriving at a surface element is given by

$$P = I_{Sun} a_{Sun} \cos(\Phi) a_{ast}/r_{ast}^2 \quad (12)$$

where I_{Sun} is the solar blackbody spectral radiation, $a_{Sun} [\text{m}^2]$ is the cross-sectional area of the Sun, $r_{ast} [\text{m}]$ is the asteroid's heliocentric distance, and Φ is the angle between the surface normal and the Sun direction. The solar radiation per solid

angle from the surface element will be P/π [$\text{W } \mu\text{m}^{-1} \text{ sr}^{-1}$] when assuming a Lambertian surface. The reflected solar radiation arriving at the 1 m^2 area summed over all visible surface elements is then:

$$f_{Sun} = \sum A \frac{P}{\pi} \cos(\Theta) \cos(\Psi) a_{ast}/r_{sc}^2. \quad (13)$$

The total spectral flux ($f_{IR} + f_{Sun}$) from a distance of 1 km can be seen in Fig. 14 for the case without eclipse with a thermal inertia of $\Gamma = 500 \text{ J m}^{-2} \text{ K}^{-1} \text{ s}^{-1/2}$.

For a better evaluation and understanding of the MER-TIS instrument performance, a simulation tool was developed, which computes the passage of the radiation from a hypothetical mineralogical surface area through the optical

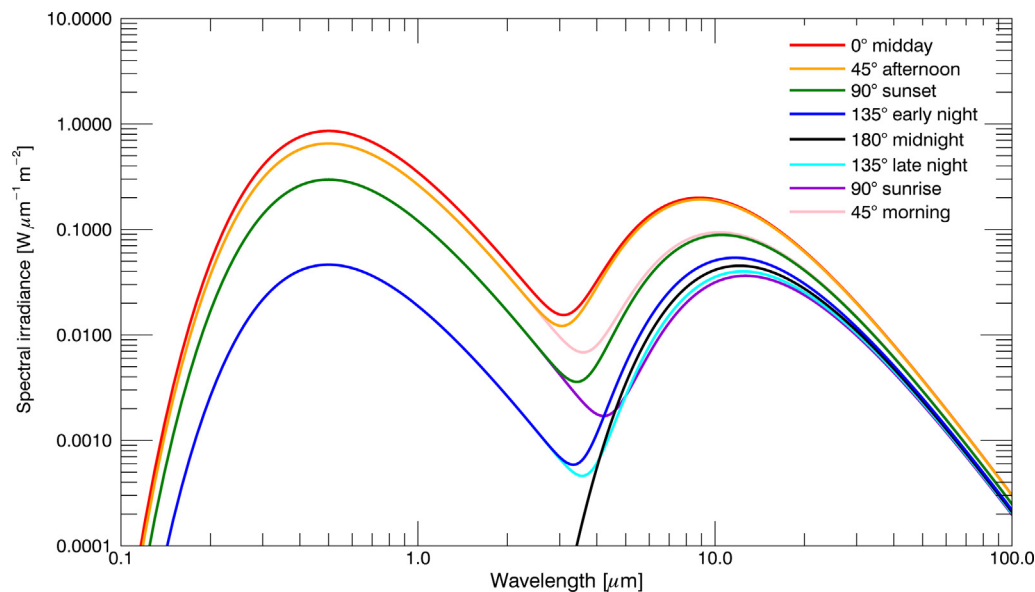


Fig. 14. The spectral irradiance at 1 km from the center of Didymoon for a thermal inertia of $\Gamma = 500 \text{ J m}^{-2} \text{ K}^{-1} \text{ s}^{-1/2}$ without eclipse at a solar distance of 1.0142 AU for different phase angles as seen by the spacecraft. This is a combination of the reflected sunlight and the thermally emitted radiation ($f_{IR} + f_{Sun}$).

system, considering the influence of the inner instrument radiation and the conversion of the overall radiation into a detector voltage and digital output signal. The goal was to provide a modular software (Paproth and Säuberlich, 2011) to enable the developers to exchange and compare experimental and simulated data within the different development stages of MERTIS, reaching from first breadboards up to the final instrument (see Fig. 15). This model has now been adapted for the TIRI instrument. The information gathered from the simulation can also support the optimization process of the instrument parameters and can assist the scientists with the analysis of scientific data from the target. A theoretical model of the infrared instrument and corresponding optical parts (Paproth et al., 2010) is used, which is necessary to estimate the instrument signal to noise ratio and spectral

resolution. The proposed TIRI resolves major terrains with a pixel size of 7 m/pixel from a 100 km distance. The single pixel SNR depends on the temperature and regolith properties of the targets. Using the spectral flux derived above or directly the surface temperatures of the thermophysical models presented in this paper as a starting point a SNR > 150 for illuminated surfaces and >15 even in the coldest conditions using a 100 ms exposure time can be expected.

While minimum and maximum temperatures are sufficient for certain estimates like the temperature range the instrument may be exposed to, a realistic observation will have a field of view covering an asteroid surface with a multitude of different temperatures. Thermophysical modeling of the complete asteroid surface provides just that and enables the investigation how a non-uniform temperature field in the instrument's field of view will affect its performance. Furthermore, the instrument's response to (daily) temperature variations can be tested.

3.3. Application to MASCOT-2 Lander

The Lander MASCOT-2 has been one of the foreseen payloads on board of the Asteroid Impact Mission. In the applied thermal mathematical model (TMM), MASCOT-2 is composed mainly of a structure carrying a foldable solar array and an isolated internal compartment hosting an electronic box collecting all electronic boards, a rechargeable battery, a communication system, two up-righting mechanisms and the payload. In this study, MASCOT-2 is analyzed in a landed configuration on the asteroid surface, with the top solar panel and LFR (Bistatic Low Frequency Radar, Herique and Ciarletti, 2016) antennas unfolded (see Fig. 16).

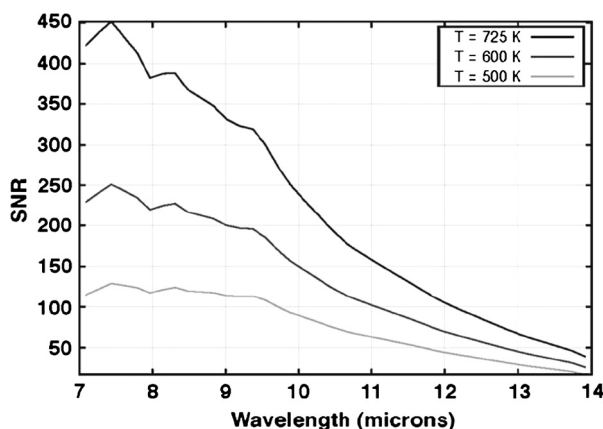


Fig. 15. Theoretical signal-to-noise ratio of the MERTIS instrument versus wavelength for different surface temperatures of Mercury, from Helbert et al. (2008).

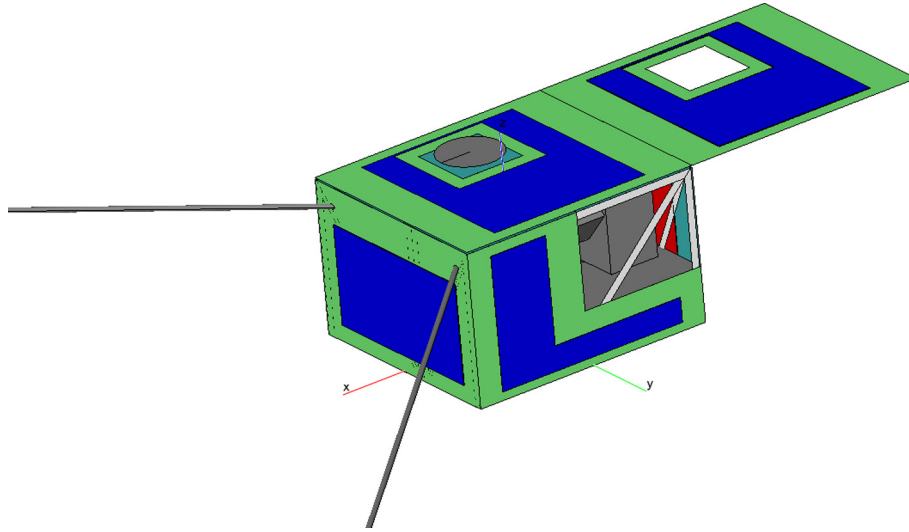


Fig. 16. MASCOT-2 Lander geometry in the TMM (size about $0.3 \times 0.3 \times 0.2 \text{ m}^3$).

Several on-asteroid cases have been analyzed, combining the following settings:

- Latitude of the landing site: $-45, -15, 0, +15, +45$ degrees.
- Longitude of the landing site: 0 degree.
- Slope (angle of inclination of the MASCOT-2 -Z side to the asteroid surface): 0 degree.
- Orientations of MASCOT-2 once in its final position: side + X facing South, West, North and East.
- Asteroid Surface Temperature Models (ASTM): Thermal Inertia $\Gamma = 50 \text{ J m}^{-2} \text{ K}^{-1} \text{ s}^{-1/2}$ and $\Gamma = 1000 \text{ J m}^{-2} \text{ K}^{-1} \text{ s}^{-1/2}$.
- Operational phases on the asteroid: Phase A (or Characterization phase) and Phase B (or Impact phase). The two phases differ mainly because of LFR operations: in Phase A LFR operates in sounding mode for a complete asteroid revolution, resulting in a quite high and long power consumption, while in Phase B LFR operates in beacon mode and its power consumption despite still high is of much shorter duration.

The investigation of the influence of the MASCOT-2 orientation on its thermal behavior has been performed for two cases, i.e. for latitudes of -15 degrees and of $+45$ degrees, both for the power profile of Phase A and a thermal inertia of $\Gamma = 1000 \text{ J m}^{-2} \text{ K}^{-1} \text{ s}^{-1/2}$. These two cases were identified, respectively, as the warmest and the coldest case after the investigation on the impact of landing site latitude, mission phase profile and asteroid thermal inertia on MASCOT-2 internal temperatures.

For the MASCOT-2 TMM in total 142 nodes have been defined, of which two isothermal nodes represent the asteroid surface (see Fig. 17):

- Asteroid surface always shadowed by the Lander itself (temperature always identical with the minimal (night) surface temperature) and
- Asteroid surface illuminated during the day (temperature defined according to a specific diurnal profile based on thermophysical model calculations as presented above).

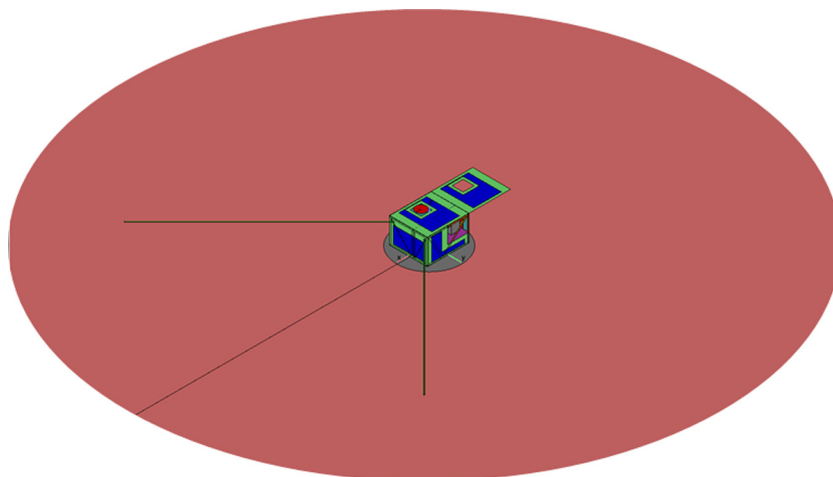


Fig. 17. Model of MASCOT-2 on an asteroid surface patch, cold area below.

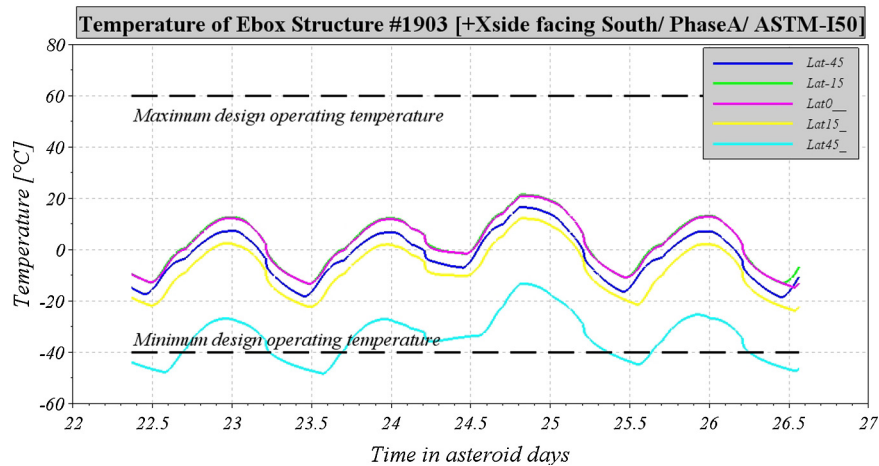


Fig. 18. Example of detailed TMM output, driven by the daily cycles of the asteroid surface temperature and illumination on the Lander.

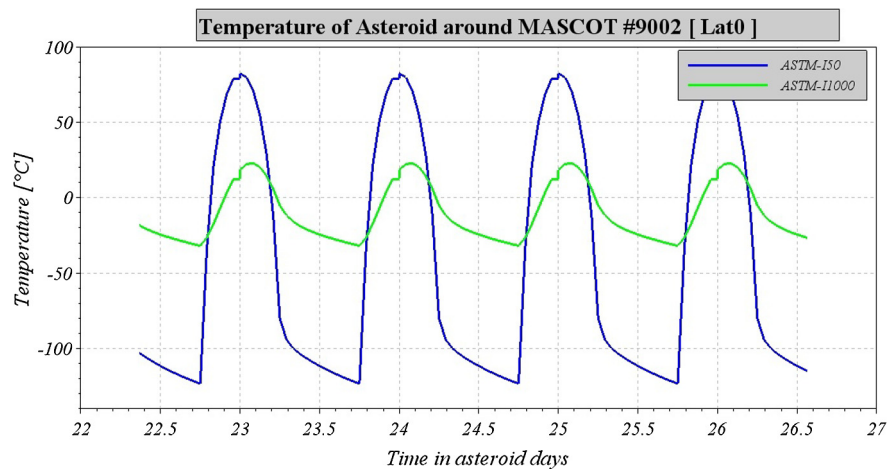


Fig. 19. Day/night temperature of asteroid for two ASTMs as seen by MASCOT-2 on the equator.

Summarizing the results, it is found that the estimated Lander temperatures are significantly different based on the thermal environment applied: latitude of selected landing site, illumination due to Lander orientation and asteroid model (thermal inertia) assumed. Fig. 18 shows a typical output of the TMM.

The ASTMs with the high and low values for thermal inertia correspond to two very different thermal environments for MASCOT-2 and their impact on the thermal behavior of the Lander has been investigated. Fig. 19 shows the different day/night temperatures of the two models for a landing site located at latitude = longitude = 0 degree: the model with lower thermal inertia ($\Gamma = 50 \text{ J m}^{-2} \text{ K}^{-1} \text{ s}^{-1/2}$) shows a higher day/night thermal excursion, as expected.

Thermal simulations show that for the internal compartment (Ebox, COMMs, Mobility and LFR electronics) the maximum daily temperatures are always below the maximum operating limit (+60 °C) and the minimum night temperatures are above the minimum operating limit (−40 °C) in all cases analyzed, except for the latitude of +45 degrees,

which is poorly illuminated and outside the LFR desired operational site latitude band. For the rechargeable battery, the maximum daily temperatures are always below the maximum operating limit (+60 °C); the minimum night temperatures stay above the minimum operating limit (−40 °C) only for latitudes around −15 degree or between −45 and 0 degree if a warm asteroid can be assumed (ASTM with thermal inertia $\Gamma = 1000 \text{ J m}^{-2} \text{ K}^{-1} \text{ s}^{-1/2}$). For the solar cells, the temperatures are always inside the operating limits [−130 °C, +120 °C] in all cases. Thus, as long as the asteroid thermal environment is not too extreme in terms of illumination and surface temperature, MASCOT-2 would have been able to survive and operate three months on Didymos' moon.

4. Summary and outlook

A thermophysical model of the secondary in the Didymos system has been established. The case study performed covers the extreme thermal inertia range of $50\text{--}1000 \text{ J m}^{-2} \text{ K}^{-1} \text{ s}^{-1/2}$ with and without shadowing

effects of the primary. Currently, calculations are based on analytical formulations of an ellipsoid. The model however can also handle shape models with triangular and quadrilateral facets in common formats. Once available, a more detailed investigation of thermal conditions can be carried out. The model is also easily adaptable to updated physics such as temperature-dependent asteroid surface properties.

Several effects have been neglected in this study, among them mutual heating between the primary and the moon, and surface roughness. However, upper limits for the effect of heating from the primary have been derived. Differences in temperature fall largely below uncertainties due to the unknown thermal inertia. For binary systems with quantified thermal inertia, especially for close systems, mutual heating should be included. The same is true for unresolved surface roughness which can change measured surface temperatures significantly.

A preliminary TIRI performance simulation has been carried out. Using the thermophysical models presented here as a starting point, covering the most extreme thermal inertia range expected, a $\text{SNR} > 150$ for illuminated surfaces and >15 even in the coldest conditions using a 100 ms exposure time has been estimated. Model updates will be used for further evaluation of the instrument's performance.

Using the thermophysical models with high and low thermal inertia of $1000 \text{ J m}^{-2} \text{ K}^{-1} \text{ s}^{-1/2}$ and $50 \text{ J m}^{-2} \text{ K}^{-1} \text{ s}^{-1/2}$ respectively, the MASCOT-2 Lander performance has been evaluated for several possible landing sites and specific settings. For these cases it has been found that temperatures are mostly within operating limits except for one case for a latitude of $+45$ degrees which, however, is outside the desired landing range.

Acknowledgement

The first author acknowledges funding by the Initiative and Networking Fund of the Helmholtz Association through the Helmholtz Postdoc Programme. We thank Matthias Grott for fruitful discussions.

References

- Asteroid impact mission: Didymos reference model. ESA reference document, v3.1, 2015.
- Bowell, E., Hapke, B., Domingue, D., Lumme, K., Peltoniemi, J., Harris, A.W., 1979. Application of photometric models to asteroids. In: Binzel, R.P., Gehrels, T., Matthews, M.S. (Eds.), *Asteroids II*, pp. 524–556.
- Davidsson, B.J.R., Rickman, H., 2014. Surface roughness and three-dimensional heat conduction in thermophysical models. *Icarus* 243, 58–77.
- Davidsson, B.J.R., Rickman, H., Bandfield, J.L., Groussin, O., Gutiérrez, P.J., Wilska, M., Capria, M.T., Emery, J.P., Helbert, J., Jorda, L., Maturilli, Mueller, T.G., 2015. Interpretation of thermal emission. I. The effect of roughness for spatially resolved atmosphereless bodies. *Icarus* 252, 1–21.
- Delbo, M., Mueller, M., Emery, J.P., Rozitis, B., Capria, M.T., 2015. Asteroid thermophysical modeling. In: Michel, P., DeMeo, F.E., Bottke, W.F. (Eds.), *Asteroids IV*. University of Arizona Press, Tucson, pp. 107–128.
- Gortas, N., Kürt, E., Motschmann, U., Keller, U., 2011. Thermal model of water and CO activity of Comet C/1995 O1 (Hale-Bopp). *Icarus* 212, 858–866.
- Helbert, J., Säuberlich, T., Paproth, C., Walter, I., Arnold, G., Hiesinger, H., 2008. MERTIS: from laboratory to mercury. In: *Infrared Spaceborne Remote Sensing and Instrumentation XVI* 7082.
- Herique, A., Ciarletti, V., 2016. A direct observation of the asteroids structure from deep interior to regolith: two radars on the AIM mission. In: *47th Lunar and Planetary Science Conference*.
- Ho, T. Mi., Baturkin, V., Grimm, C., et al., 2016. MASCOT – the mobile asteroid surface scout onboard the Hayabusa2 mission. *Space Sci. Rev.*, 1–36.
- Kitazato, K., Abe, M., Mito, H., Tarusawa, K., Soyano, T., Nishihara, S., Sarugaku, Y., 2004. Photometric behaviour dependent on solar phase angle and physical characteristics of binary near-earth-asteroid (65803) 1996 GT. In: *35th Lunar and Planetary Science Conference*, March 15–19, 2004, League City, Texas, abstract no. 1623.
- Kührt, E., Giese, B., 1989. A thermal model of the Martian satellites. *Icarus* 81, 102–112.
- Kührt, E., Giese, B., Keller, H.U., Ksanfomality, L.V., 1992. Interpretation of the KRFM-infrared measurements of PHOBOS. *Icarus* 96, 213–218.
- Margot, J.-L., Pravec, P., Taylor, P., Carry, B., Jacobson, S., 2015. Asteroid systems: binaries, triples, and pairs. In: Michel, P., DeMeo, F.E., Bottke, W.F. (Eds.), *Asteroids IV*, pp. 355–374.
- Michel, P., Cheng, A., Küppers, M., Pravec, P., Blum, J., Delbo, M., Green, S.F., Rosenblatt, P., Tsiganis, K., Vincent, J.B., Biele, J., Ciarletti, V., Hérique, A., Ulamec, S., Carnelli, I., Galvez, A., Benner, L., Naidu, S.P., Barnouin, O.S., Richardson, D.C., Rivkin, A., Scheirich, P., Moskovitz, N., Thirouin, A., Schwartz, S.R., Campo Bagatin, A., Yu, Y., 2016. Science case for the Asteroid Impact Mission (AIM): a component of the asteroid impact & deflection assessment (AIDA) mission. *Adv. Space Res.* 57, 2529–2547.
- Paproth, Säuberlich, T., 2011. MERTIS: identifiability of spectral mineralogical features in dependence of the signal to noise ratio. In: *Proc. SPIE 8154, Infrared Remote Sensing and Instrumentation XIX*, 815412.
- Paproth, C., Säuberlich, T., Jahn, H., Helbert, J., 2010. MERTIS: system theory and simulation. In: *Proc. SPIE 7808, Infrared Remote Sensing and Instrumentation XVIII*, 78080M.
- Pravec, P., Benner, L.A.M., Nolan, M.C., Kusnirak, P., Pray, D., Giorgini, J.D., Jurgens, R.F., Ostro, S.J., Margot, J.-L., Magri, C., Grauer, A., Larson, S., 2003. (65803) 1996 GT, *IAU Circ.*, 8244, 2.
- Pravec, P., Scheirich, P., Kušnirák, P., et al., 2006. Photometric survey of binary near-Earth asteroids. *Icarus* 181, 63–93.
- Sekanina, Z., 1979. Fan-shaped coma, orientation of rotation axis, and surface structure of a cometary nucleus. I. Test of a model on four comets. *Icarus* 37, 420–442.
- Walter, I., Zeh, T., Helbert, J., Hiesinger, H., Gebhardt, A., Hirsch, H., Knollenberg, J., Kessler, E., Rataj, M., Habermeier, J., Kaiser, S., Peter, G., 2011. Deep space instrument design for thermal infrared imaging with MERTIS. In: *Proc. SPIE 8154, Infrared Remote Sensing and Instrumentation XIX*, 81540Y.